

High-fidelity geometric quantum gates exceeding 99.9% in germanium quantum dots

Zhou, Yu Chen; Ma, Rong Long; Kong, Zhenzhen; Li, Ao Ran; Zhang, Chengxian; Zhang, Xin; Liu, Yang; Jiang, Hao Tian; Guo, Guo Ping; More Authors

DOI

[10.1038/s41467-025-63241-4](https://doi.org/10.1038/s41467-025-63241-4)

Publication date

2025

Document Version

Final published version

Published in

Nature Communications

Citation (APA)

Zhou, Y. C., Ma, R. L., Kong, Z., Li, A. R., Zhang, C., Zhang, X., Liu, Y., Jiang, H. T., Guo, G. P., & More Authors (2025). High-fidelity geometric quantum gates exceeding 99.9% in germanium quantum dots. *Nature Communications*, 16(1), Article 7953. <https://doi.org/10.1038/s41467-025-63241-4>

Important note

To cite this publication, please use the final published version (if applicable).
Please check the document version above.

Copyright

Other than for strictly personal use, it is not permitted to download, forward or distribute the text or part of it, without the consent of the author(s) and/or copyright holder(s), unless the work is under an open content license such as Creative Commons.

Takedown policy

Please contact us and provide details if you believe this document breaches copyrights.
We will remove access to the work immediately and investigate your claim.

High-fidelity geometric quantum gates exceeding 99.9% in germanium quantum dots

Received: 5 March 2025

Accepted: 12 August 2025

Published online: 26 August 2025

 Check for updates


Yu-Chen Zhou^{1,2}, Rong-Long Ma^{1,2}, Zhenzhen Kong^{3,4}, Ao-Ran Li^{1,2}, Chengxian Zhang⁵, Xin Zhang⁶, Yang Liu^{1,2}, Hao-Tian Jiang^{1,2}, Zhi-Tao Wu^{1,2}, Gui-Lei Wang^{3,4,7} , Gang Cao^{1,2,7} , Guang-Can Guo^{1,2,7}, Hai-Ou Li^{1,2,7}  & Guo-Ping Guo^{1,2,7,8} 

Achieving high-fidelity and robust qubit manipulations is a crucial requirement for realizing fault-tolerant quantum computation. Here, we demonstrate a single-hole spin qubit in a germanium quantum dot and characterize its control fidelity using gate set tomography. The maximum control fidelities reach 97.48%, 99.81%, 99.88% for the I , $X/2$ and $Y/2$ gate, respectively. These results reveal that off-resonance noise during consecutive I gates in gate set tomography sequences severely limits qubit performance. Therefore, we introduce geometric quantum computation to realize noise-resilient qubit manipulation. The geometric gate control fidelities remain above 99% across a wide range of Rabi frequencies. The maximum fidelity surpasses 99.9%. Furthermore, the fidelities of geometric $X/2$ and $Y/2$ (I) gates exceed 99% even when detuning the microwave frequency by ± 2.5 MHz (± 1.2 MHz), highlighting the noise-resilient feature. These results demonstrate that geometric quantum computation is a potential method for achieving high-fidelity qubit manipulation reproducibly in semiconductor quantum computation.

Spin qubits based on semiconductor quantum dots¹ are considered among the most promising candidates for building blocks in quantum computers^{2,3}. Among various quantum-dot types, hole spins in germanium combine several features favorable for encoding qubits⁴, including all-electrical control based on intrinsic spin-orbit interaction^{5–8}, low effective mass that simplifies fabrication⁹, and reduced hyperfine interaction attributed to atomic p orbitals⁴ and the abundance of net-zero nuclear spin isotopes^{6,8}. Recently, significant developments have been made, including high-quality single- and two-qubit gates^{10–13}, singlet-triplet qubits operating at much lower magnetic field^{14–16} and a 4×4 two-dimensional crossbar

quantum-dot array with fine tunability¹⁷. Despite these achievements, a persistent issue is that strong spin-orbit interaction is a double-edged sword, enabling ultrafast qubit control while exposing the qubit to complex noise environments^{4,18}. In addition, anisotropic susceptibility to noise results in site-dependent qubit properties and nonuniform qubit operations, posing significant obstacles for large-scale quantum computation¹³. As the number of qubits scales up, semiconductor quantum computation is entering the noisy intermediate-scale quantum (NISQ) era, which demands increasingly stringent requirements for noise-resilient, uniform, and high-fidelity operations across dense arrays¹⁹. Therefore, it is a

¹Key Laboratory of Quantum Information, University of Science and Technology of China, Hefei, Anhui, China. ²CAS Center for Excellence in Quantum Information and Quantum Physics, University of Science and Technology of China, Hefei, Anhui, China. ³Integrated Circuit Advanced Process R&D Center, Institute of Microelectronics, Chinese Academy of Sciences, Beijing, China. ⁴Beijing Superstring Academy of Memory Technology, Beijing, China. ⁵School of Physical Science and Technology, Guangxi University, Nanning, China. ⁶QuTech and Kavli Institute of Nanoscience, Delft University of Technology, Delft, The Netherlands. ⁷Hefei National Laboratory, Hefei, China. ⁸Origin Quantum Computing Company Limited, Hefei, Anhui, China.

 e-mail: guilei.wang@bjsamt.org.cn; haiouli@ustc.edu.cn; gpguo@ustc.edu.cn

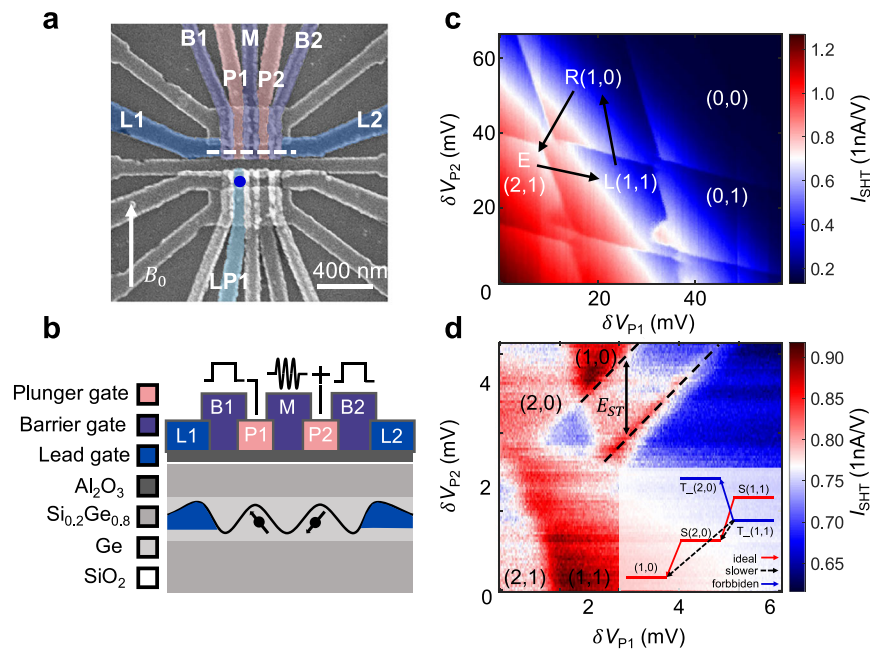


Fig. 1 | Device fabrication and experimental setup. **a** False-colored SEM images of the device. The upper side is the DQD's structure, and the lower region serves as a charge sensor (blue circle). **b** Cross-section schematic of the device along the white dashed line in (a). Holes confined under gate P1 and P2 can tunnel to the reservoir under gate L1 and L2, with the tunnel rates adjusted by barrier gates B1 and B2. Square pulses and microwave pulses are applied to gates P1 and P2 for state readout

and manipulation. **c** Charge stability diagram of DQDs. (N1, N2) represent the number of holes in the quantum dot under gate P1 and P2. Points E, L, and R represent the relative position of square pulses for ELR. **d** The latching region for ELR is indicated by parallel black dashed lines, where the distance corresponds to E_{ST} . Inset: energy level and state-ladder schematic at the latching region.

paramount challenge to improve error robustness while maintaining high-quality qubit operation²⁰.

As a seminal and enduring example, geometric quantum computation (GQC) continues to attract significant attention in the field of quantum computation^{21–24}. Compared to dynamical phases, geometric phases are determined by the geometry of the evolution path and are immune to perturbations that do not change the enclosed area of the path^{25,26}, indicating their robustness against certain types of noise^{27,28}. Taking advantage of geometric phases, geometric quantum gates can achieve noise-resilient operations. Early GQC proposals utilized adiabatic evolution to suppress unwanted transitions and state leakage^{22,29–31}. However, coherence times are typically much shorter than the evolution times of adiabatic geometric gates, rendering this approach universally impractical for quantum computation. To speed up gate manipulation while still retaining robustness, nonadiabatic geometric quantum computation (NGQC) has been proposed and demonstrated. Depending on the dimension of the governing Hamiltonian and energy level configurations^{22,32}, geometric gates are classified as Abelian-phase-based^{33–35} or non-Abelian-phase-based^{23,36}. Notably, Abelian-phase NGQC features experimental simplicity and feasibility, paving a promising way toward universal quantum computation³⁷. As a two-level system, hole spin qubits are well-suited for implementing NGQC schemes based on Abelian phases, benefiting from ultrafast qubit manipulations¹² and easy fabrication of two-dimensional lattice structures¹¹. By designing specific evolution paths, NGQC demonstrates the robustness against off-resonance noise (Larmor frequency noise) and systematic noise (Rabi frequency noise)^{38,39}. Despite the implementation of Abelian-phase geometric quantum gates, their noise-resilient feature remains unverified, and the control fidelities remain far below the threshold for fault-tolerant semiconductor quantum computation^{24,40}. Nevertheless, achieving high-fidelity, noise-resilient qubit manipulation is essential for the practical application of GQC in scalable quantum computing.

Here, we establish a hole spin qubit based on a strained germanium quantum dot. We achieve a 19 MHz Rabi frequency with a qubit

dephasing time of $T_2^* = 136$ ns, which can be extended to $6.75 \mu\text{s}$ through dynamical decoupling techniques. To evaluate qubit control performance, we benchmark single-qubit gate control fidelities at a series of Rabi frequencies f_{Rabi} utilizing gate set tomography (GST)⁴¹. The control fidelities of both the $X/2$ gate and $Y/2$ gate approach $\sim 99.9\%$ as the Rabi frequency increases, while those of I gate saturate at 97.48% , which reveals that off-resonance noise seriously affects qubit control fidelity⁴². Furthermore, to remove obstacles caused by noise, we introduce nonadiabatic geometric gates based on Abelian geometric phases to implement noise-resilient quantum gates^{37,43}. To clearly compare the performance of GQC with that of dynamical gates, we characterize the control fidelities of geometric gates across a wide range of Rabi frequencies. The geometric gate control fidelities always remain above 99%, demonstrating uniform and high-quality qubit manipulation. Notably, the maximum fidelity can reach 99.9%, satisfying the demand for quantum error correction using surface code⁴⁴. Moreover, we experimentally demonstrate the noise-resilient feature of geometric quantum gates by detuning the microwave frequency away from the qubit frequency. The control fidelities of geometric $X/2$ and $Y/2$ (I) gates can still reach 99% with the microwave frequency detuned by ± 2.5 MHz (± 1.2 MHz), highlighting their role in reducing the need for frequent qubit frequency calibration^{37,45}. Our results reveal that GQC is a convincing method for achieving reliable and high-fidelity qubit control in complex noise environments.

Results

Measurement techniques

Figure 1a presents a false-colored scanning electron microscope (SEM) image of a double quantum dots (DQDs) device fabricated on an undoped strained germanium wafer⁴⁶. The fabrication details are similar to those described in ref. 47. The device consists of two sections: the upper part is configured as the DQDs, and the lower portion (blue circle) serves as a charge sensor to detect the charge configuration of DQDs. An external in-plane magnetic field B_0 of 1333 mT is

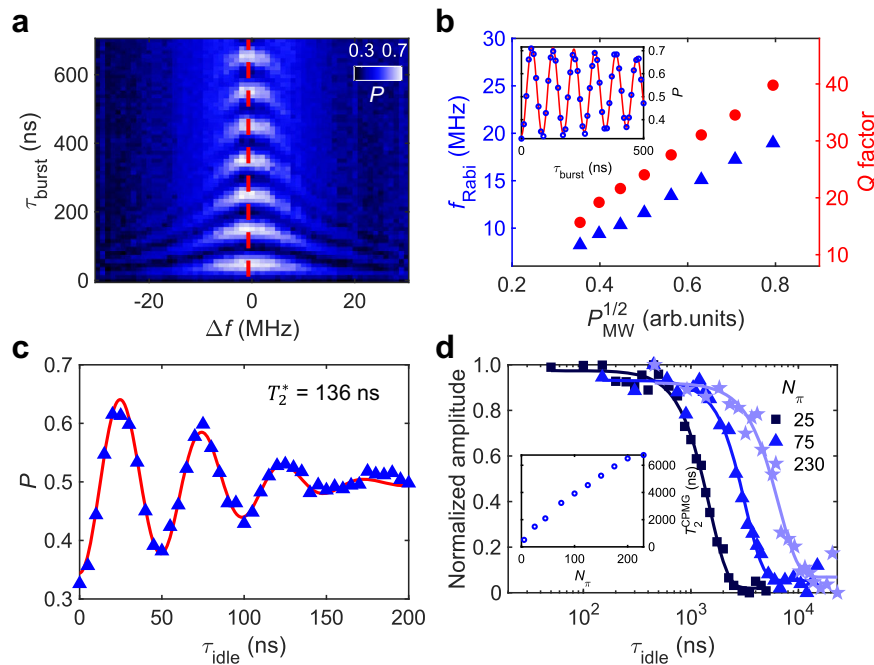


Fig. 2 | Qubit properties. **a** The Rabi chevron pattern: singlet state probability P_S as a function of τ_{burst} and Δf . **b** Rabi frequency (blue triangles) and the Q factor (red circles) measured under different microwave power $P_{\text{MW}}^{1/2}$, showing no saturation. The largest f_{Rabi} of 19 MHz and Q factor of 39.78 are achieved. Inset: P_S as a function of τ_{burst} along the red dashed line in (a). The red solid line represents the fitting

result, yielding a Rabi frequency of 11.56 MHz and Q factor of 18.04. **c** Ramsey fringe obtained by varying the idle time τ_{idle} , with the fitted dephasing time T_2^* of 136 ns. The red solid line represents the fitting result. **d** Coherence decay under CPMG sequences as a function of total idle time for different N_π . Inset: T_2^{CPMG} as a function of N_π . For the largest $N_\pi = 230$, we obtain $T_2^{\text{CPMG}} = 6.75 \mu\text{s}$.

applied to provide Zeeman splitting for defining spin qubits. Figure 1b shows a cross-section schematic of the DQDs along the white dashed line in Fig. 1a. The hole spins are confined in DQDs by selectively tuning the plunger gates P1 and P2, as well as barrier gates. Additionally, the tunnel coupling between the quantum dots and their reservoirs, and inter-dot tunnel coupling can be modified separately via three barrier gates B1, B2, and M. We apply microwave pulses to gate P2, and three-step pulses to gates P1 and P2 to initialize, control and readout the qubit state (see the “Methods” section for details). Detected by the charge sensor, the charge stability diagram of DQDs is depicted in Fig. 1c, where N_i represents the number of holes in the quantum dot under gate P_i , respectively. We select the (1, 1)–(2, 0) inter-dot tunneling region for spin state readout via enhanced latching readout (ELR)⁴⁸, which is based on Pauli spin blockade (PSB)⁴⁹. The latching phenomenon originates from the asymmetric coupling strengths between the two dots and their adjacent reservoirs⁴⁸. By tuning the voltage on gate B2, the tunnel rate between the dot beneath P2 and the right reservoir beneath L2 can be pinched off (Supplementary Note 1), forcing holes in the dot beneath P2 to tunnel into the left reservoir via co-tunneling with the dot beneath P1, a process that also occurs slowly.

The ELR process is explained by comparing the theoretical latching behaviors when the spin state is initialized as a singlet or triplet state⁵⁰. The energy levels and state-ladder schematic in the latching region are shown in the inset of Fig. 1d, where only the singlet state S and the ground triplet state T_- are considered for simplification. If $T_-(1, 1)$ is initialized, it cannot tunnel into $S(2, 0)$ due to PSB, or into $T_-(2, 0)$ due to insufficient energy. Direct tunneling into (1, 0) is suppressed due to a slow tunnel rate, resulting in no detectable signal in the latching region. In contrast, the singlet state tunnels to (1, 0) via (2, 0) state, thereby generating a full-hole signal. Therefore, the singlet and triplet states can be clearly distinguished by monitoring hole tunneling from the dot beneath P1 to the left reservoir. The following experiments employ single-shot ELR. Figure 1c illustrates the cyclic E–L–R pulse sequence used to probe the latching region. The spin state is initialized into an $S-T$

mixed state at stage L via the transition from (2, 1) to (1, 1). Scanning the voltage of stage R within the range shown in Fig. 1d, the latching region in (1, 0) becomes visible, as depicted by parallel black dashed lines. The energy difference between the singlet and triplet states is 0.8 meV, determined by a lever arm of 0.13 eV V^{-1} (see Supplementary Note 2).

Qubit Properties

Next, we focus on coherent qubit control. The spin state is initialized into T_- at stage L by waiting for a sufficiently long period (see Supplementary Note 3). Qubit operations are performed via electric dipole spin resonance (EDSR) mediated by the intrinsic spin–orbit interaction (SOI)^{6,12}. When the microwave frequency (f_{MW}) matches the qubit resonance frequency, T_- is operated to S and PSB is lifted. Consequently, a full-hole signal can be detected at stage R^{48,50}. By applying a rectangular-shaped microwave burst (τ_{burst}) with a fixed duration of t_π (time for a π rotation), two resonance frequencies $f_1 = 5.60 \text{ GHz}$ and $f_2 = 7.53 \text{ GHz}$ are measured (Supplementary Note 4). Using the relation $hf_i = g_i \mu_B B_0$, g -factors $g_1 = 0.29$ and $g_2 = 0.39$ are extracted, where h is Planck’s constant and μ_B is the Bohr magneton. In the following measurements, we mainly focus on the qubit with the higher frequency and characterize its properties⁸. Firstly, Fig. 2a shows the Rabi chevron pattern by varying τ_{burst} and Δf (defined as $f_{\text{MW}} - f_2$). Along the red dashed line where f_{MW} resonates with f_2 (inset of Fig. 2b), the hole spin rotates over an angle determined by τ_{burst} . Fitting the oscillation yields Rabi frequency $f_{\text{Rabi}} = 11.56 \text{ MHz}$, $T_2^{\text{Rabi}} = 1.56 \mu\text{s}$, and a quality factor $Q = 18.04$ (defined by $2 * T_2^{\text{Rabi}} * f_{\text{Rabi}}$). As shown in Fig. 2b, increasing driving power continuously, both f_{Rabi} and the Q factor rise monotonically without saturation, as indicated by the blue triangles and red circles, respectively. At maximum driving power, f_{Rabi} reaches 19 MHz with the highest $Q = 39.78$. To characterize the qubit dephasing time T_2^* , we perform a Ramsey experiment with $\Delta f = 20 \text{ MHz}$. By varying the idle time (τ_{idle}) between two $X/2$ pulses, the Ramsey decay (see Fig. 2c) yields a dephasing time $T_2^* = 136 \text{ ns}$ at $f_{\text{Rabi}} = 11.56 \text{ MHz}$. T_2^* remains nearly constant across the measured f_{Rabi} range (Supplementary

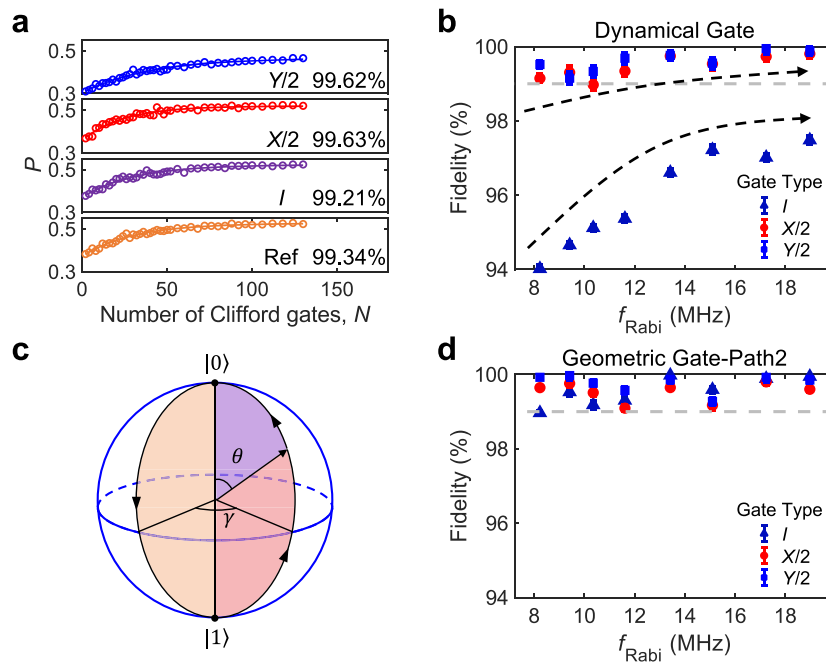


Fig. 3 | Control fidelity and geometric quantum computation. **a** Sequence fidelities for reference (abbreviated as “Ref”) and each interleaved characterized by RB, where N represents the number of Clifford gates in the reference sequences. The control fidelity is shown below the corresponding curves. **b** The control fidelities of the dynamical gate set extracted by GST as a function of f_{Rabi} . The black dashed arrows guide the eyes, indicating the tendency of the fidelity. The light gray line represents the 99% control fidelity threshold. As the Rabi frequency increases, the control fidelities of $X/2$ and $Y/2$ gates gradually improve to nearly 99.9%,

whereas the I gate control fidelity saturates at 97.48%. Error bars represent the 95% confidence level. **c** The schematic of the evolution path Path2. **d** The control fidelities of the geometric gate Path2 as a function of f_{Rabi} . The average control fidelity exceeds 99% at each f_{Rabi} , demonstrating the superiority of geometric gates. The light gray line denotes the 99% control fidelity threshold, consistent with panel **b**. The data points consistently exceed the reference line at each f_{Rabi} . This demonstrates the superior performance of the geometric gates. Error bars represent the 95% confidence level.

Note 5). Furthermore, we apply the Carr–Purcell–Meiboom–Gil (CPMG) sequence to alleviate the effect of noise and extend the coherence time⁵¹, in which a series of Y gates are inserted between two $X/2$ operations to refocus the qubit state⁵². Figure 2d shows a set of normalized signals with a coherence time T_2^{CPMG} of 6.75 μs for $N_\pi = 230$ (N_π denotes the number of Y gates in the CPMG sequence), which is 50 times longer than T_2^* . As shown in the inset of Fig. 2d, T_2^{CPMG} increases linearly with N_π , which indicates that low-frequency noise is one of the important noise sources, as revealed through the equivalent filter functions of the CPMG pulse sequence^{13,51,53}.

Control fidelity

Among the various quantum benchmarking techniques, randomized benchmarking (RB)⁵⁴ and gate set tomography (GST)^{41,55} stand out for their robustness against state preparation and measurement (SPAM) errors. We therefore implement both techniques to accurately assess the qubit control fidelity. RB experiment employs two types of sequences: reference sequences and interleaved sequences. The reference sequence consists of N random Clifford gates and an additional recovery gate that recovers the spin to the spin-down state. The interleaved sequences, created by inserting the target gate between adjacent random gates of the reference sequences, are used to evaluate the control fidelity of the target gate (more details shown in Supplementary Note 6). Figure 3a shows the control fidelities of single-qubit gates measured using RB. The average single-qubit gate fidelity is 99.49%, with both I , $X/2$ and $Y/2$ gate control fidelities exceeding 99%—surpassing the threshold for quantum error correction using surface codes⁴⁴. Here, the I gate denotes an identity operation implemented by idling for the duration of a $\pi/2$ X or Y rotation. For GST, the default gate set contains I , $X/2$ and $Y/2$ gates. GST sequences consist of two components: fiducials for state preparation and germs for amplifying various types of gate errors. The number of total sequences depends on

sequence depth. We select a sequence depth of 8, yielding a total of 448 GST sequences. Each sequence is constructed by interleaving these fiducials with germ sequences, after which we measure the singlet state probability (more details shown in Supplementary Note 6). Analyzed by the Python package pyGSTi, Fig. 3b presents the single-qubit gate fidelities across different f_{Rabi} characterized by GST⁵⁶. Gate fidelities show a positive correlation with f_{Rabi} , in agreement with the Q factor trend shown in Fig. 2b. The best performance occurs at $f_{\text{Rabi}} = 19$ MHz, achieving control fidelity of 97.48% for I gate, 99.81% for $X/2$ gate and 99.88% for $Y/2$ gate. Note that the I gate fidelities remain substantially below 99% across the entire f_{Rabi} range, which is mainly due to the shorter T_2^* compared to the idle time composed of multiple consecutive I gates in the GST sequence. On the one hand, the infidelity owing to Rabi decay is small, as indicated by the high-fidelity (99.49% on average) single-qubit gate characterized by RB²⁰. On the other hand, some pulse sequences in the GST experiment include idle times much longer than T_2^* , which mainly limits the control fidelity⁵⁷. Raising f_{Rabi} directly helps suppress the effect of dephasing^{11,20}. As a result, the control fidelity of I gate improves 3.46% and those of $X/2$ and $Y/2$ gate are much closer to 99.9%. Unfortunately, when f_{Rabi} exceeds 15 MHz, the I gate fidelity appears to saturate but is still significantly below 99%. Table 1 lists the control fidelities of dynamical gates characterized by RB and GST at $f_{\text{Rabi}} = 19$ MHz, which are similar to each other except for the I gate. This discrepancy arises from the differences in sequence composition between the two methods (see Supplementary Note 6)¹¹.

Geometric quantum computation

Analysis of the error generator in GST reveals that the errors can be classified into coherent Hamiltonian errors and incoherent stochastic errors^{58,59}. For coherent errors, diverse strategies can be employed to mitigate them, such as dynamical decoupling or recalibrating control^{58–60}. For stochastic errors, such as dephasing and depolarizing

noise, we propose a noise-resilient operation strategy to counteract uncorrelated noise⁵⁸. We introduce GQC, a technique known for its superior robustness^{37,61} to resist various noises, enabling uniform and high-fidelity qubit manipulation.

We consider a Hamiltonian for a two-level qubit system driven by a classical microwave field,

$$H = \frac{\hbar}{2} \begin{pmatrix} \Delta f & (1 + \delta)f_{\text{Rabi}} e^{-i\Phi} \\ (1 + \delta)f_{\text{Rabi}} e^{i\Phi} & -\Delta f \end{pmatrix}, \quad (1)$$

where Δf represents the difference between f_{MW} and f_2 . The corresponding terms appear in the diagonal elements of the Hamiltonian. The fluctuations in f_{Rabi} , δ , manifest in the off-diagonal elements of the Hamiltonian. To construct nonadiabatic single-qubit geometric gates, the evolution loop is designed as a closed trajectory consisting of three intervals in the experiment: $0 \rightarrow \tau_1, \tau_1 \rightarrow \tau_2, \tau_2 \rightarrow \tau_3$. During each interval, the microwave has different phases and amplitudes, as detailed below.

$$\begin{aligned} \int_0^{\tau_1} 2\pi f_{\text{Rabi}} dt &= \theta, \Phi(t) = \phi - \pi/2, t \in [0, \tau_1], \\ \int_{\tau_1}^{\tau_2} 2\pi f_{\text{Rabi}} dt &= \pi, \Phi(t) = \phi + \gamma - \pi/2, t \in [\tau_1, \tau_2], \\ \int_{\tau_2}^{\tau_3} 2\pi f_{\text{Rabi}} dt &= \pi - \theta, \Phi(t) = \phi - \pi/2, t \in [\tau_2, \tau_3]. \end{aligned} \quad (2)$$

The formulas above describe one of the proposals to realize a geometric gate, labeled as “Path2” in the following (see the evolution path shown in Fig. 3c). An alternative proposal, labeled as “Path1”, replaces the phase of the second interval with $\Phi(t) = \phi + \gamma + \pi/2$. These two proposals target different types of noise. Path1 addresses systematic noise δ , which represents fluctuations of f_{Rabi} , while Path2 resists off-resonance noise Δf , defined by the fluctuations of f_2 ³⁷.

Following the cyclic evolution loop above, the equivalent evolution operator is

$$\begin{aligned} U(\theta, \gamma, \phi) &= \cos \gamma + i \sin \gamma \begin{pmatrix} \cos \theta & \sin \theta e^{-i\phi} \\ \sin \theta e^{i\phi} & -\cos \theta \end{pmatrix} \\ &= \exp(i\gamma \mathbf{n} \cdot \boldsymbol{\sigma}), \end{aligned} \quad (3)$$

Table 1 | The fidelity of the dynamical single-qubit gate set

	Ref.	I	X/2	Y/2
RB (%)	99.34(8)	99.21(3)	99.63(2)	99.62(2)
GST (%)	–	97.48(9)	99.81(9)	99.88(8)

which determines the rotation around the axis $\mathbf{n} = (\sin \theta \cos \phi, \sin \theta \sin \phi, \cos \theta)$ by an angle -2γ , where $\boldsymbol{\sigma}$ represents the Pauli operators. An arbitrary single-qubit geometric gate can be achieved by adjusting the parameters in the evolution loop. For example, by setting $\theta = \pi/2, \phi = \pi/2, \gamma = 0$, a geometric I gate is obtained. This geometric I gate effectively implements a 2π rotation about x -axis through three steps.

Figure 3d presents the control fidelities of single-qubit geometric gates Path2 as a function of f_{Rabi} , analyzed through GST. In contrast to dynamical gates, the average fidelities of geometric gates exceed 99% throughout the entire measurement range, highlighting the superiority of GQC. The maximum control fidelities reach 99.98%, 99.80%, and 99.97% for the $I, X/2$, and $Y/2$ gates, respectively. The detailed data shown in Fig. 3d are provided in Supplementary Table I. Especially, the fidelity of the I gate can be significantly improved even when f_{Rabi} is small. Unlike Path2, the control fidelity of the gate set achieved by Path1 is well below 99% (Supplementary Note 11). This is probably because the systematic noise targeted by Path1 is relatively weaker than the off-resonance noise here (Supplementary Note 8)^{24,62,63}. To simultaneously resist both types of noise, we introduce an enhanced geometric gate featuring a 3π evolution path (named Path3 π) that extends 1.5 times longer than Path1 and Path2³⁸. However, its performance is significantly worse than that of Path2, probably due to the longer operation time (see Supplementary Note 9).

Noise-resilient operation

After realizing high-fidelity single-qubit geometric gates, we further demonstrate their noise-resilient characteristics against Δf . As shown in the upper panels of Fig. 4, we compare the performance of the Δf -error-affected geometric gate (red triangles) with that of the corresponding dynamical counterparts (“Dyn” for short, blue circles). As expected, the gate set implemented with geometric gate Path2 is clearly superior to the conventional dynamical gate. The fidelities of the geometric $X/2$ and $Y/2$ (I) gates exceed 99% even when $\Delta f = \pm 2.5$ MHz (± 1.2 MHz). Furthermore, Δf measurements over 55 h fall precisely within this range, verifying the ability of the geometric gate to alleviate the need for frequent calibration of qubit resonance frequency (Supplementary Note 10). Moreover, the lower panels of Fig. 4 show the differences in control fidelities between the geometric and dynamical gates. As $|\Delta f|$ increases, the fidelities of the dynamical gate decrease faster than those of the geometric gate, which confirms that the geometric gate is more robust against off-resonant noise. Additionally, the robustness against Rabi error δ is displayed by comparing Path1 with the dynamical gate in Supplementary Note 11. In order to explain the noise-resilient feature of the geometric gate, we

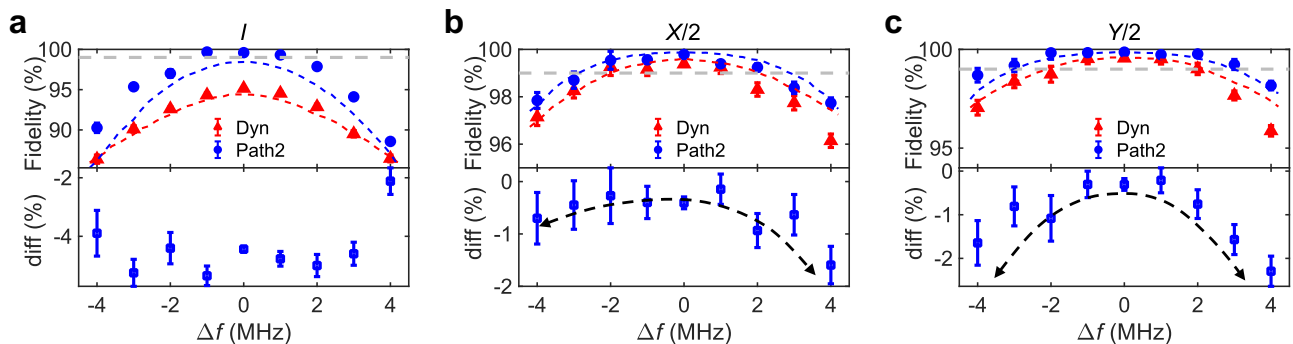


Fig. 4 | Noise-resilient feature of single-qubit geometric gates. The upper panels of **a–c** show that control fidelities of the $I, X/2$ and $Y/2$ gates, realized by both geometric and dynamical approaches, as a function of Δf . The light gray lines represent a 99% control fidelity threshold. Notably, even with detuning Δf by ± 2.5 MHz (± 1.2 MHz), the control fidelities of geometric $X/2$ and $Y/2$ (I) gates can still reach 99%. The differences in the control fidelities between the two approaches are

displayed in the lower panels. The black dashed arrows serve as visual guides to emphasize that as Δf increases, the control fidelities of the dynamical gates decrease faster than those of the geometric gate. Error bars represent the 95% confidence level. The experimental results are consistent with the numerical simulations (blue and red dashed lines).

numerically simulate the fidelity with additional off-resonance noise. Based on the T_2^* values and the GST report, we choose an appropriate noise strength as the starting point. We then calculate the probability of the singlet state for each GST sequence and analyze the fidelity. By numerical simulation, the final parameters we extracted are $\delta f^{\text{armor}} = 1.80$ MHz and $\delta f^{\text{Rabi}} = 58.48$ kHz. The calculated fidelities, overlaid in Fig. 4 (Supplementary Note 7), show that the theoretical results align with the experimental results in terms of overall trends. These results clearly demonstrate the advantages of GQC in achieving high-fidelity qubit manipulations despite the presence of complex noise.

Discussion

For the practical implementation of geometric quantum gates, two necessary considerations are optimal scheme selection and geometric gate operation time. The geometric gates we have implemented are tailored for different noise types. Therefore, the best scheme choice depends on the specific noise experienced by spin qubits. In semiconductor quantum computation, the dominant noise source depends on the wafer material, device architecture, and frequency domain of interest⁶⁴. Through characterization of qubit coherence time, noise spectrum analysis^{65,66}, report analyzed by gate set tomography⁵⁹ or the envelope of Rabi oscillation decay⁶⁷, we can make a basic assessment of noise type and noise level, enabling the efficient selection of the optimal geometric gate scheme. Otherwise, counterproductive effects may arise (Supplementary Note 8). Depending on the relative strengths of systematic and off-resonance noise, we can choose either Path1 or Path2. When the strengths of off-resonance noise and systematic noise are comparable, alternative protocols such as Path3 π or nonadiabatic geometric quantum computation with noncyclic evolution paths can be employed⁶⁸. On the other hand, the evolution times of all types of geometric gates implemented here are four or six times longer than those of dynamical gates. There is a trade-off between extended operation time and enhanced noise resistance. Encouragingly, a noncyclic nonadiabatic geometric quantum gate was recently proposed to shorten the evolution time, effectively avoiding the cumulative disturbances of errors due to excessive time consumption^{35,68}.

Regarding the practical advantages of geometric gate applications, reproducible high-fidelity qubit control without frequent recalibration of control parameters is particularly attractive. In current devices with a limited number of qubits, calibration requires a considerable amount of time^{20,66,69}. Although improvements in circuit optimization and fabrication techniques can help mitigate the noise strengths, complete elimination of noise remains challenging. Expanding to large-scale quantum computation, the varying noise environments experienced by individual qubits pose significant challenges to reproducibly achieving high-fidelity qubit control. As calibration becomes increasingly resource-demanding, it significantly hinders the efficiency of the qubit processors. Geometric gates can potentially reduce both the time and resource consumption required for recalibration in large-scale quantum computation.

In conclusion, we characterize the single-hole spin qubit in germanium DQDs and extract its control fidelity via GST. Along with increasing f_{Rabi} and the Q factor, the fidelities of the dynamical gate gradually saturated, and those of $X/2$ and $Y/2$ approach $\sim 99.9\%$. However, for the I gate, the fidelity remains significantly below 99% which indicates the susceptibility of the spin qubit to off-resonance noise. In order to explore a strategy for achieving noise-resilient and high-fidelity spin qubit manipulation in future large-scale quantum computation, we introduce GQC featuring noise robustness. Two different geometric evolution loops, named Path1 and Path2, are implemented to specifically deal with systematic and off-resonance noise, respectively. Regarding geometric gate Path2, the average control fidelity of the gate set consistently reaches 99% across a wide range of f_{Rabi} ,

demonstrating its potential to achieve uniform qubit control under various situations. In addition, the I , $X/2$, and $Y/2$ gates exhibit maximum control fidelities of 99.98%, 99.80%, and 99.97%, respectively, despite requiring four times the operation time of dynamical gates. Furthermore, we demonstrate the robustness of geometric gates by adding off-resonance noise Δf , which currently has a more harmful impact on qubit properties. The error-affected performance of Path2 is superior to that of dynamical gates throughout the entire measurement. Calibration of the qubit resonance frequency in experiments is a time-intensive and resource-demanding process. The geometric gate, despite detuning Δf by ± 2.5 MHz (± 1.2 MHz), still achieves fidelities of the $X/2$ and $Y/2$ (I) gates that reach fault-tolerant quantum computing thresholds, confirming its ability to perform high-fidelity and noise-resilient qubit operations while alleviating the need for frequent qubit frequency calibration. Consequently, the demonstrated geometric quantum gate has broad application prospects for implementing high-fidelity and robust qubit manipulations for large-scale quantum computation. Moreover, in future work, combined with two-qubit geometric gates^{37,70}, it is expected to realize robust universal geometric quantum computation in a large-scale qubit array.

Methods

We perform the experiments using an Oxford dry dilution refrigerator with a base temperature of -15 mK. A three-stage gate voltage pulse is generated by an arbitrary waveform generator (AWG Keysight M8190). The pulse is combined with the DC-voltages using an analog summing amplifier (SRS SIM980) and applied to plunger gates, which are connected to the DC-port of a commercial bias tee (Anritsu K251). Meanwhile, leveraging I/Q modulated signals from Tektronix AWG5208 channel pairs, we apply a microwave signal generated by a vector signal generator (Keysight E8267D) connected to the RF IN port of the bias tee. The microwave pulse modulation, generated by the AWG5208, is turned on 500 ns before and turned off 500 ns after the microwave signal. By measuring the current of the single-hole transistor, we can detect the qubit state by a charge sensing technique. Being amplified by a room-temperature amplifier (SRS SR570 and SR560), the output current can be digitized by a PCI-based waveform digitizer (AlazarTech ATS 9440) at a sampling rate of 5 MSa/s.

Data availability

The data used in this study are available in the Zenodo database under accession code <https://doi.org/10.5281/zenodo.16450274>. Source data are provided with this paper.

Code availability

Error taxonomy was performed with the pyGSTi package^{56,59}. All other supporting algorithms are provided in the main text and Supplementary Material through equations.

References

1. Loss, D. & DiVincenzo, D. P. Quantum computation with quantum dots. *Phys. Rev. A* **57**, 120–126 (1998).
2. Zhang, X. et al. Semiconductor quantum computation. *Natl. Sci. Rev.* **6**, 32–54 (2019).
3. Stano, P. & Loss, D. Review of performance metrics of spin qubits in gated semiconducting nanostructures. *Nat. Rev. Phys.* **4**, 672–688 (2022).
4. Scappucci, G. et al. The germanium quantum information route. *Nat. Rev. Mater.* **6**, 926–943 (2020).
5. Liu, H. et al. Ultrafast and electrically tunable Rabi frequency in a germanium hut wire hole spin qubit. *Nano Lett.* **23**, 3810–3817 (2023).
6. Wang, K. et al. Ultrafast coherent control of a hole spin qubit in a germanium quantum dot. *Nat. Commun.* **13**, 206 (2022).

7. Watzinger, H. et al. A germanium hole spin qubit. *Nat. Commun.* **9**, 3902 (2018).
8. Hendrickx, N. W. et al. A four-qubit germanium quantum processor. *Nature* **591**, 580–585 (2021).
9. Lodari, M. et al. Light effective hole mass in undoped Ge/SiGe quantum wells. *Phys. Rev. B* **100**, 041304 (2019).
10. Lawrie, W. I. L. et al. Simultaneous single-qubit driving of semiconductor spin qubits at the fault-tolerant threshold. *Nat. Commun.* **14**, 3617 (2023).
11. Wang, C.-A. et al. Operating semiconductor quantum processors with hopping spins. *Science* **385**, 447–452 (2024).
12. Hendrickx, N., Franke, D., Sammak, A., Scappucci, G. & Veldhorst, M. Fast two-qubit logic with holes in germanium. *Nature* **577**, 487–491 (2020).
13. Hendrickx, N. W. et al. Sweet-spot operation of a germanium hole spin qubit with highly anisotropic noise sensitivity. *Nat. Mater.* **23**, 920–927 (2024).
14. Jirovec, D. et al. A singlet–triplet hole spin qubit in planar Ge. *Nat. Mater.* **20**, 1106–1112 (2021).
15. Zhang, X. et al. Universal control of four singlet–triplet qubits. *Nat. Nanotechnol.* **20**, 209–215 (2025).
16. Rooney, J. et al. Gate modulation of the hole singlet–triplet qubit frequency in germanium. *npj Quantum Inf.* **11**, 15 (2025).
17. Borsoi, F. et al. Shared control of a 16 semiconductor quantum dot crossbar array. *Nat. Nanotechnol.* **19**, 21–27 (2024).
18. Wang, Z. et al. Optimal operation points for ultrafast, highly coherent Ge hole spin–orbit qubits. *npj Quantum Inf.* **7**, 54 (2021).
19. Preskill, J. Quantum computing in the NISQ era and beyond. *Quantum* **2**, 79 (2018).
20. Noiri, A. et al. Fast universal quantum gate above the fault-tolerance threshold in silicon. *Nature* **601**, 338–342 (2022).
21. Pachos, J., Zanardi, P. & Rasetti, M. Non-Abelian Berry connections for quantum computation. *Phys. Rev. A* **61**, 010305 (1999).
22. Duan, L.-M., Cirac, J. I. & Zoller, P. Geometric manipulation of trapped ions for quantum computation. *Science* **292**, 1695–1697 (2001).
23. Zu, C. et al. Experimental realization of universal geometric quantum gates with solid-state spins. *Nature* **514**, 72–75 (2014).
24. Ma, R.-L. et al. Single-spin-qubit geometric gate in a silicon quantum dot. *Phys. Rev. Appl.* **21**, 014044 (2024).
25. Aharonov, Y. & Anandan, J. Phase change during a cyclic quantum evolution. *Phys. Rev. Lett.* **58**, 1593–1596 (1987).
26. Zhu, S.-L. & Zanardi, P. Geometric quantum gates that are robust against stochastic control errors. *Phys. Rev. A* **72**, 020301 (2005).
27. De Chiara, G. & Palma, G. M. Berry phase for a spin 1/2 particle in a classical fluctuating field. *Phys. Rev. Lett.* **91**, 090404 (2003).
28. Carollo, A., Fuentes-Guridi, I., Santos, M. F. & Vedral, V. Spin-1/2 geometric phase driven by decohering quantum fields. *Phys. Rev. Lett.* **92**, 020402 (2004).
29. Victor, B. M. Quantal phase factors accompanying adiabatic changes. *Proc. R. Soc. Lond. A* **392**, 45–57 (1984).
30. Wilczek, F. & Zee, A. Appearance of gauge structure in simple dynamical systems. *Phys. Rev. Lett.* **52**, 2111–2114 (1984).
31. Huang, Y.-Y. et al. Experimental realization of robust geometric quantum gates with solid-state spins. *Phys. Rev. Lett.* **122**, 010503 (2019).
32. Mousolou, V. A., Canali, C. M. & Sjöqvist, E. Universal non-adiabatic holonomic gates in quantum dots and single-molecule magnets. *New J. Phys.* **16**, 013029 (2014).
33. Zhu, S.-L. & Wang, Z. D. Implementation of universal quantum gates based on nonadiabatic geometric phases. *Phys. Rev. Lett.* **89**, 097902 (2002).
34. Zhu, S.-L. & Wang, Z. D. Unconventional geometric quantum computation. *Phys. Rev. Lett.* **91**, 187902 (2003).
35. Yang, X.-X. et al. Experimental implementation of short-path non-adiabatic geometric gates in a superconducting circuit. *Phys. Rev. Appl.* **19**, 044076 (2023).
36. Yan, T. et al. Experimental realization of nonadiabatic shortcut to non-Abelian geometric gates. *Phys. Rev. Lett.* **122**, 080501 (2019).
37. Zhang, C., Chen, T., Li, S., Wang, X. & Xue, Z.-Y. High-fidelity geometric gate for silicon-based spin qubits. *Phys. Rev. A* **101**, 052302 (2020).
38. Guo, L.-J. et al. Optimizing nonadiabatic geometric quantum gates against off-resonance error in a silicon-based spin qubit. *Phys. Rev. A* **107**, 012604 (2023).
39. Chen, T., Xue, Z.-Y. & Wang, Z. Error-tolerant geometric quantum control for logical qubits with minimal resources. *Phys. Rev. Appl.* **18**, 014062 (2022).
40. Wang, L., Tu, T., Gong, B., Zhou, C. & Guo, G.-C. Experimental realization of non-adiabatic universal quantum gates using geometric Landau–Zener–Stückelberg interferometry. *Sci. Rep.* **6**, 19048 (2016).
41. Nielsen, E. et al. Gate set tomography. *Quantum* **5**, 557 (2021).
42. Mehmandoust, M. & Dobrovitski, V. V. Decoherence induced by a sparse bath of two-level fluctuators: peculiar features of $1/f$ noise in high-quality qubits. *Phys. Rev. Res.* **6**, 033175 (2024).
43. Xu, Y. et al. Experimental implementation of universal nonadiabatic geometric quantum gates in a superconducting circuit. *Phys. Rev. Lett.* **124**, 230503 (2020).
44. Fowler, A. G., Mariantoni, M., Martinis, J. M. & Cleland, A. N. Surface codes: towards practical large-scale quantum computation. *Phys. Rev. A* **86**, 032324 (2012).
45. Berritta, F. et al. Physics-informed tracking of qubit fluctuations. *Phys. Rev. Appl.* **22**, 014033 (2024).
46. Kong, Z. et al. Undoped strained Ge quantum well with ultrahigh mobility of two million. *ACS Appl. Mater. Interfaces* **15**, 28799–28805 (2023).
47. Zhang, X. et al. Giant anisotropy of spin relaxation and spin-valley mixing in a silicon quantum dot. *Phys. Rev. Lett.* **124**, 257701 (2020).
48. Harvey-Collard, P. et al. High-fidelity single-shot readout for a spin qubit via an enhanced latching mechanism. *Phys. Rev. X* **8**, 021046 (2018).
49. Johnson, A. C. et al. Triplet–singlet spin relaxation via nuclei in a double quantum dot. *Nature* **435**, 925–928 (2005).
50. Ma, R.-L. et al. Singlet-triplet-state readout in silicon metal-oxide-semiconductor double quantum dots. *Phys. Rev. Appl.* **21**, 034022 (2024).
51. Cywiński, u, Lutchyn, R. M., Nave, C. P. & Das Sarma, S. How to enhance dephasing time in superconducting qubits. *Phys. Rev. B* **77**, 174509 (2008).
52. Veldhorst, M. et al. An addressable quantum dot qubit with fault-tolerant control-fidelity. *Nat. Nanotechnol.* **9**, 981–985 (2014).
53. Mądzik, M. T. et al. Controllable freezing of the nuclear spin bath in a single-atom spin qubit. *Sci. Adv.* **6**, eaba3442 (2020).
54. Knill, E. et al. Randomized benchmarking of quantum gates. *Phys. Rev. A* **77**, 012307 (2008).
55. Blume-Kohout, R. et al. Demonstration of qubit operations below a rigorous fault tolerance threshold with gate set tomography. *Nat. Commun.* **8**, 14485 (2017).
56. Nielsen, E. et al. Probing quantum processor performance with pyGSTi. *Quantum Sci. Technol.* **5**, 044002 (2020).
57. Xue, X. et al. Quantum logic with spin qubits crossing the surface code threshold. *Nature* **601**, 343–347 (2022).
58. Huang, E., Doherty, A. C. & Flammia, S. Performance of quantum error correction with coherent errors. *Phys. Rev. A* **99**, 022313 (2019).
59. Blume-Kohout, R. et al. A taxonomy of small Markovian errors. *PRX Quantum* **3**, 020335 (2022).

60. Dehollain, J. P. et al. Optimization of a solid-state electron spin qubit using gate set tomography. *New J. Phys.* **18**, 103018 (2016).
61. Chen, T., Hu, J.-Q., Zhang, C. & Xue, Z.-Y. Universal robust geometric quantum control via geometric trajectory correction. *Phys. Rev. Appl.* **22**, 014060 (2024).
62. Kawakami, E. et al. Gate fidelity and coherence of an electron spin in an Si/SiGe quantum dot with micromagnet. *Proc. Natl Acad. Sci. USA* **113**, 11738–11743 (2016).
63. Yang, C. H. et al. Silicon qubit fidelities approaching incoherent noise limits via pulse engineering. *Nat. Electron.* **2**, 151–158 (2019).
64. Burkard, G., Ladd, T. D., Pan, A., Nichol, J. M. & Petta, J. R. Semiconductor spin qubits. *Rev. Mod. Phys.* **95**, 025003 (2023).
65. Yoneda, J. et al. A quantum-dot spin qubit with coherence limited by charge noise and fidelity higher than 99.9%. *Nat. Nanotechnol.* **13**, 102–106 (2018).
66. Dumoulin Stuyck, N. et al. Silicon spin qubit noise characterization using real-time feedback protocols and wavelet analysis. *Appl. Phys. Lett.* **124**, 114003 (2024).
67. Nakajima, T. et al. Coherence of a driven electron spin qubit actively decoupled from quasistatic noise. *Phys. Rev. X* **10**, 011060 (2020).
68. Ma, Z. et al. Noncyclic nonadiabatic geometric quantum gates in a superconducting circuit. *Phys. Rev. Appl.* **20**, 054047 (2023).
69. Phillips, S. G. J. et al. Universal control of a six-qubit quantum processor in silicon. *Nature* **609**, 919–924 (2022).
70. Lu, Y.-Y., Wei, K. & Zhang, C. Geometric two-qubit gates in silicon-based double quantum dots. *Phys. Rev. A* **111**, 042609 (2025).
- and G.C. helped prepare the manuscript. H.-O.L. and G.-P.G. supervised the project.

Competing interests

The authors declare no competing interests.

Additional information

Supplementary information The online version contains supplementary material available at <https://doi.org/10.1038/s41467-025-63241-4>.

Correspondence and requests for materials should be addressed to Gui-Lei Wang, Hai-Ou Li or Guo-Ping Guo.

Peer review information *Nature Communications* thanks Tao Chen, David W. Kanaar, and the other, anonymous, reviewer for their contribution to the peer review of this work. A peer review file is available.

Reprints and permissions information is available at <http://www.nature.com/reprints>

Publisher's note Springer Nature remains neutral with regard to jurisdictional claims in published maps and institutional affiliations.

Open Access This article is licensed under a Creative Commons Attribution-NonCommercial-NoDerivatives 4.0 International License, which permits any non-commercial use, sharing, distribution and reproduction in any medium or format, as long as you give appropriate credit to the original author(s) and the source, provide a link to the Creative Commons licence, and indicate if you modified the licensed material. You do not have permission under this licence to share adapted material derived from this article or parts of it. The images or other third party material in this article are included in the article's Creative Commons licence, unless indicated otherwise in a credit line to the material. If material is not included in the article's Creative Commons licence and your intended use is not permitted by statutory regulation or exceeds the permitted use, you will need to obtain permission directly from the copyright holder. To view a copy of this licence, visit <http://creativecommons.org/licenses/by-nc-nd/4.0/>.

© The Author(s) 2025

Acknowledgements

This work was supported by the National Natural Science Foundation of China (Grant Nos. 92165207, 12474490, 12034018, 92265113, and 62404248), the Innovation Program for Quantum Science and Technology (Grant No. 2021ZD0302300). This work was partially carried out at the USTC Center for Micro and Nanoscale Research and Fabrication.

Author contributions

Y.-C.Z. performed the bulk of the measurement and data analysis with the help of R.-L.M. Y.-C.Z. fabricated the device with the help of Y.L., H.-T.J., and Z.-T.W. Z.-Z.K. and G.-L.W. supplied the planar germanium heterostructure. Y.-C.Z. wrote the manuscript with inputs from other authors. A.-R.L. provided theoretical support and contributed to the simulation. H.-O.L., C.-X.Z., and G.-C.G. advised on experiments. X.Z.